Research Article

Fractional-Order Active Disturbance Rejection Controller Design for Large Radio Telescope Antenna

Jian-Yu Jiang, Bin Wu, and Ting Zhou [ID]

School of Mechanical, Electronic and Control Engineering, Beijing Jiaotong University, Beijing 100044, China

Correspondence should be addressed to Ting Zhou; 14116373@bjtu.edu.cn

large radio telescope antennas are required in current astronomical research and deep space communication applications. The wind disturbance becomes a serious problem with an increase in the size of the antennas. Based on the typical antenna model, this work aims to design a fractional-order active disturbance rejection controller (FOADRC) for improving the accuracy of the antenna pointing mechanism in wind disturbance. First, the fractional-order active disturbance rejection control scheme is chosen to estimate and compensate both the wind disturbance and other uncertain mechanical dynamics. Afterwards, the relationship between the parameters of fractional-order extended state observer and the performance of disturbance suppression and noise immunity is revealed. The stability of fractional-order extended state observer is proved under similar assumptions as an integer order extended state observer. In addition, a stability region boundary calculation method is presented to simplify the parameter setting procedure. Finally, we perform simulations to verify the superiority of FOADRC in the antenna control system under wind disturbance. The results demonstrate that FOADRC has a good capability of resisting wind disturbance; at the same time, it limits the response overshoot and converges faster compared to other industrial controllers.

1. Introduction

Large radio telescopes are indispensable for studying various phenomena, such as planet formation, black holes, and dark energy in the universe. Green Bank Telescope is the world's largest fully steerable telescope (100 m) that was built in America in 2001. China also plans to build a 110 m fully steerable telescope antenna called the Qitai radio telescope (QTT) [1, 2]. In the case of large antennas, the total pointing error is mainly decided by the disturbance caused by winds [3]. The methods used for reducing the effect of disturbance caused by winds have garnered a great deal of research attention in the past half-century. Some of these methods presented in the previous literature [4–7] include building an antenna in a small valley or in a radome, enhancing the stiffness of the structure, and using mesh reflector antennas. However, all of these methods degrade the performance of antennas.

The control compensation is recognized as the most appropriate method for mitigating wind disturbance. In order to provide the groundwork for controller design, Gawronski developed three wind models, which are confirmed based on the experimental results [8]. The PI controllers are widely used, but are reckoned to be undesirable since they are unable to meet the stringent pointing requirements. NASA [9] investigated the relationships between the antenna performance parameters as a function of controller gains and applied the relationship to the NASA Deep Space Network antennas with dish sizes of 34 or 70 meters. However, for a 65 m antenna with a PI controller, the required pointing accuracy cannot be achieved if the speed of wind is greater than 10 m/s. Therefore, implementing the LQG algorithm yields a substantial improvement in tracking precision, as presented in Gawronski's study regarding the impact of the weights of a closed-loop bandwidth antenna, disturbance rejection properties, and antenna acceleration. Gawronski also presented the tuning procedure of the controller based on the coordinate selection and the weight properties [10]. In addition, the author also designed and analyzed an LQG controller for NASA's Deep Space

Network antennas and executed the new control algorithms on an DSS-13 antenna. The experimental results showed an improvement in the performance of the LQG over the existing PI controller [11]. Yu-Xuan et al. proposed an LQG controller with Kalman optimal estimation to address the pointing inaccuracy of the deep space antenna due to gust disturbances [12]. For a traditional 34-m Cassegrain antenna servo system, Hu et al. designed an LQG controller with wind-gust disturbance rejection capability by virtue of state estimation and optimal feedback control. The simulation results show that the LQG controller has satisfactory results [13]. Gawronski discussed PI, LQG, and H_{∞} algorithms and their basic properties, tracking precision, and limitations of the NASA Deep Space Network antenna-control systems. The obstacle to applying LQG or H_{∞} algorithms to antenna control system is the acceleration limits on existing antenna drives, i.e., the motors and gearboxes [14].

Similar to the PID algorithm, the advanced control algorithms without an accurate model are another way to improve the performance of the antenna control system. These algorithms only require modifications in certain software for making them more practical and computationally efficient. Since its inception, the active disturbance rejection control (ADRC) [15] has been used in various devices, such as motion control, DC-DC power converter, chemical processes, micro-electro-mechanical systems gyroscope, and attitude tracking of rigid spacecraft, and has achieved superior performance [16]. The ADRC offers a new and inherently robust controller building block by using an ESO to estimate both the internal plant dynamics and external disturbances. Gao proposed LADRC to avoid the repetitive controller tuning process for plants that differ mainly in terms of gain and bandwidth [17]. Qiu et al. designed LADRC for a large deep space observatory antenna by considering the wind load torque and other uncertain mechanical dynamics as total disturbances and then used ESO to estimate and compensate the total estimated disturbances. The effectiveness of the proposed approach was illustrated based on mathematical formulations and experiments [18]. Yuan et al. analyzed stability, rejection quality for external disturbance, and robustness for uncertainty, as well as noise sensitivity characteristics based on a closed-loop transfer function and frequency response [19]. Wu et al. improved the tuning efficiency with a new method to calculate the stability of regions based on D-partition, as evidenced by the digital simulations and an experiment performed using a water tank [20].

The fractional-order control is another easy-to-deploy technique for improving the systems involving PID algorithms. It has been used in various applications since Podlubny proposed fractional PID controllers in 1994 [21]. It not only benefits automatic voltage regulation, permanent magnet synchronous motor speed servo systems, small fixed-wing unmanned aerial vehicle, and dc-motor with elastic shaft but also helps the designers to achieve robust performance in flexible spacecraft attitude control [22]. The stability of a certain class of fractional-order linear and nonlinear systems is investigated in [23]. Hamamci

presented a method to stabilize a given fractional-order system with time delay using the D-decomposition method. This algorithm is simple and has reliable result illustrated by an example [24]. Li proposed generalized Mittag–Leffler stability and studied the stability of fractional-order nonlinear dynamic systems using the Lyapunov direct method [25]. Chen et al. presented a fractional-order active disturbance rejection control with a fractional-order extended state observer for the permanent magnet synchronous motor speed servo system. The simulations and experiments show that the proposed FOADRC performs better as compared to the integer order ADRC and FOPI controller [26]. Li et al. proposed a fractional active disturbance rejection control scheme by generalizing the traditional extended states' observer to a fractional-order extended states' observer. Simulation results by the fractional active disturbance rejection control and ADRC on the typical fractional-order system are compared to demonstrate the superiority and effectiveness of the proposed scheme [27]. Sheikh et al. propose a novel fractional active disturbance rejection controller for the combined operation of load frequency control and automatic voltage regulator of a hybrid power system. The robustness of the controller gains is tested under different system parameter changes from their nominal values. Results show that the developed controller operates encouragingly with reference to system stability, rapidity, and accuracy in comparison to testified control strategies available in [28].

In this work, the fractional-order control integrated with active disturbance rejection control is designed for achieving high pointing accuracy in case of large radio telescope antennas under wind disturbances. The main contributions of this work are summarized:

(1) The application of fractional-order active disturbance rejection control for large radio telescope antennas under wind disturbances. The core is to consider the wind disturbance and the difference between the antenna model and the standard model as the total disturbance, so as to estimate and compensate the total disturbance using FOADRC.

(2) The stability of FOESO is proved by using the Lyapunov method. The rejection quality of external disturbance and noise sensitivity characteristics of FOADRC is studied.

(3) The stability region of FOADRC is determined by D-composition. The FOADRC controller for 25 m antenna is designed, and its effectiveness is verified based on simulations.

The rest of the study is organized as follows.

The models of the antenna control system and wind disturbance are presented in Section 2. FOADRC for antenna is presented in Section 3. Section 4 presents the rigorous proof of stability of FOESO. In addition, the effect of parameters on FOESO performance is also analyzed in this section. Section 5 analyzes stability of FOADRC along with a detailed computation approach for the stability region as well as results. Section 6 conducts an effectiveness test of

the designed FOADRC controller based on numerical simulations. Section 7 concludes this work.

2. Modeling of Antennas and Wind Disturbance

The modeling of antennas and wind disturbance are explained in the following sections.

2.1. Large Antenna Precision Servo Control System. The antenna control system includes an antenna structure, motor, reducer, amplifiers, current sensor, tachometer, encoder, and controllers. As shown in Figure 1, the mechanical equations of the antenna control system consist of three parts, namely, the loop voltage equation of motor, torque balance of the motor and reducer, and torque balance of reducer and antenna structure.

The mechanical equations of the antenna control system are expressed as follows:

$$
\begin{cases}
U_a = e + R_a I_a + L_a \dfrac{dI_a}{dt}, \\[2mm]
e = K_e \dot{\theta}_m, \\[2mm]
2K_m I_a = \dfrac{1}{N} M_L + 2J_m \ddot{\theta}_m, \\[2mm]
J_a \ddot{\theta}_a = 2K_g \left(\dfrac{1}{N} \theta_m - \theta_a \right),
\end{cases}
\tag{1}
$$

where U_a, R_a, L_a, I_a denote the voltage, resistance, inductance, and current of the armature, respectively, e denotes the back electromotive force, K_e denotes the back electromotive force constant, J_m, J_a represent the motor inertia and antenna inertia, respectively, θ_m and θ_a represent the angular positions of the motor and the antenna shaft, K_m denotes the motor torque constant, K_g denotes the equivalent stiffness of the output shaft of a single-chain gearbox and the antenna shaft, N denotes the gearbox turn ratio, and M_L denotes the mechanical load torque on the dish. The traditional three-loop control strategy is presented in Figure 2. Please note that the controllers for speed and current loops are PI controllers. It is difficult to change these controllers because they are integrated with analog circuits. The position loop controller can be easily modified as its operations are software based. The plant of the position controller is represented by the blue region in Figure 2.

The position loop transfer function of the 35-m antenna presented in [29] is expressed as follows:

$$
G(s) = \frac{\theta_a}{U_g} = \frac{19.712s + 111.736}{s^5 + 6.54s^4 + 151s^3 + 580s^2 + 1370s},
\tag{2}
$$

where θ_a denotes the angular position of the antenna and U_g denotes the position control voltage.

2.2. Wind Disturbance Models. It is well known that the wind is the main source of antenna disturbance. It disturbs the antenna structure and causes pointing errors. The velocity of the wind gust is regarded as the input. The gust component is a random process with zero mean and a spectrum called Davenport spectrum. The Davenport spectrum is mathematically expressed as follows:

$$
S_v(\omega) = 4800 v_m k \frac{\beta \omega}{\left(1 + \beta^2 \omega^2\right)^{4/3}},
$$
$$
\beta = \frac{600}{\pi v_m},
\tag{3}
$$
$$
k = \frac{1}{\left[2.5 \ln \left(z/z_0\right)\right]^2},
$$

where v_m denotes the mean velocity, z denotes the distance between the antenna reflector center and the ground, and z_0 denotes the height of the terrain roughness. In the simulations, a fourth-order filter named the Davenport filter is used to approximate the Davenport spectrum as

$$
H(s) = \frac{3.9021s^3 + 230.1426s^2 - 686.3151s + 3.4197}{0.331s^4 + 38.2997s^3 + 224.7118s^2 + 22.7788s + 0.3538}.
\tag{4}
$$

The approximate effect of the Davenport filter is presented in Figure 3. It has very small errors in the target frequency band. The wind-gust torque is mathematically expressed as follows:

$$
M_\omega = k_t \Delta v_0,
$$
$$
\Delta v_0 = \frac{\Delta v}{\alpha v_m},
$$
$$
k_t = \frac{c_t \alpha_p \alpha \pi D^3 v_m^2}{2N},
\tag{5}
$$
$$
\alpha = \sqrt{6k},
$$

where c_t denotes the torque coefficient, a_p denotes the static air density, and D denotes the diameter of antenna. For a wind with a velocity of 8.94 m/s, $k_t = 23553.4849 m^2/s^2$.

The torque is filtered by using a filter F that outputs a velocity, which is added to the velocity input of the antenna:

$$
F(s) = \frac{s}{k_d},
\tag{6}
$$

where k_d denotes the drive gain. For this antenna, the drive gain is $k_d = 1.1 \times 10^8 \text{Nms/deg}$. The final wind velocity is presented in Figure 4.
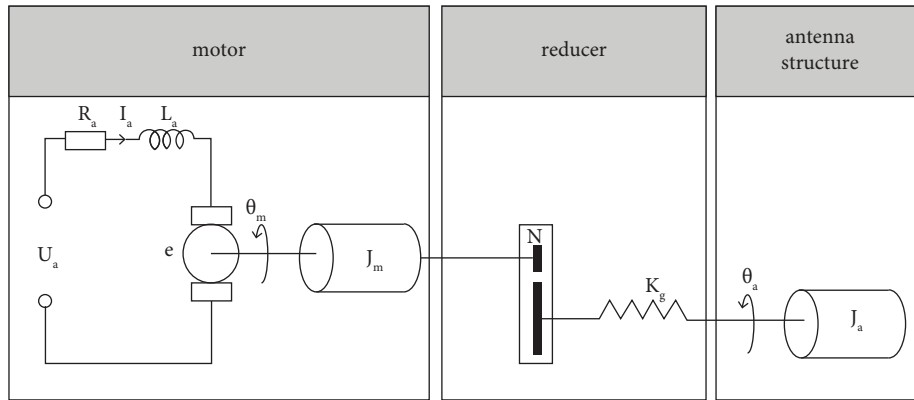
FIGURE 1: Main components of the antenna servo control system and their relationship.
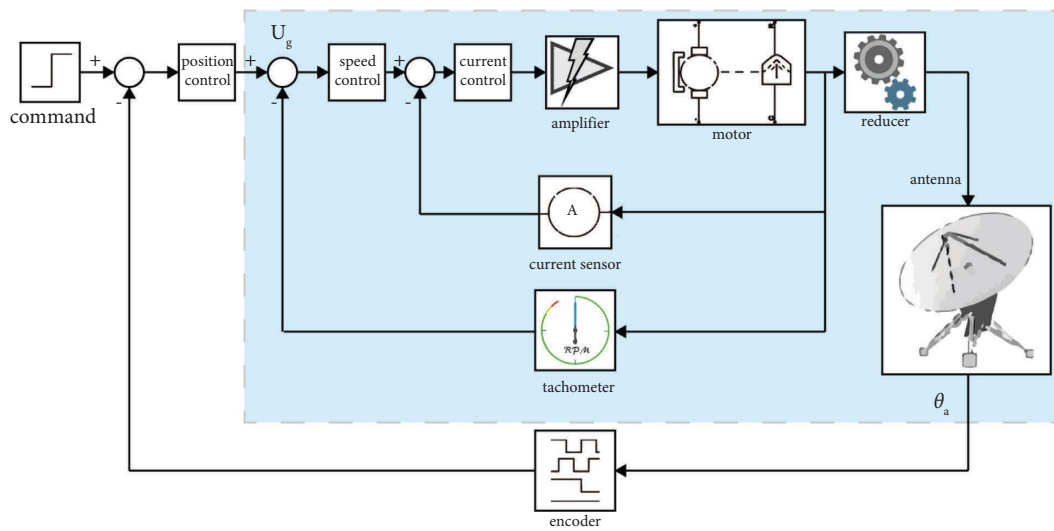

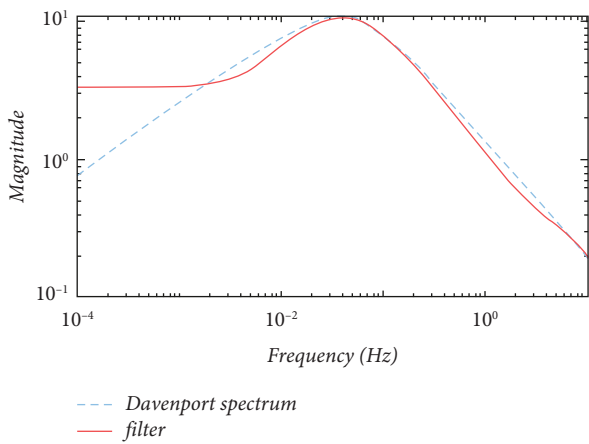FIGURE 2: The three-loop control structure of the antennas.

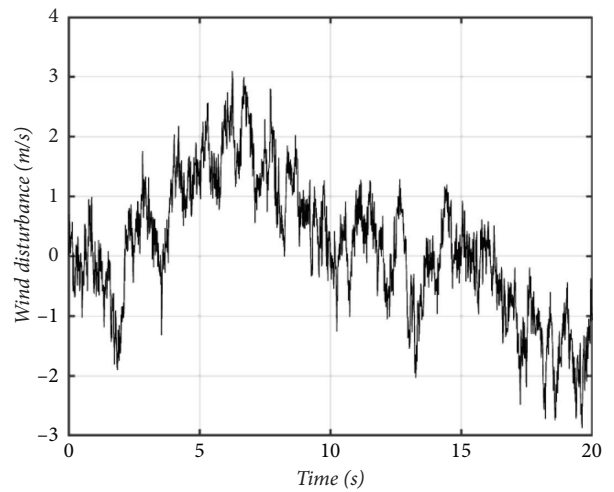FIGURE 3: The square root of the Davenport spectrum and magnitude-frequency curve of the filter.

FIGURE 4: The wind velocity generated using the Davenport filter.

3. Fractional-Order Active Disturbance Rejection Position Control Design for Antenna

The fractional-order active disturbance rejection position control design for antenna is explained in the following sections.

3.1. Preliminaries of Fractional Calculus and Fractional Control. The fractional-order calculus plays an important role in many complex scientific problems. In this section, we introduce the definitions and properties of fractional-order control used in this work.

The uniform formula of a fractional integral with $\alpha \in (0, 1)$ is defined as follows [30]:

$$_aD_t^{-a}f(t) = \frac{1}{\Gamma(\alpha)} \int_a^t \frac{f(\tau)}{(t-\tau)^{1-\alpha}}, \tag{7}$$

where $f(t)$ denotes an arbitrary integrable function, α denotes the integral order, a and t denote the lower and upper limits of the fractional-order integral, respectively, and $\Gamma(\cdot)$ denotes the Gamma function. For an arbitrary real number p, the Riemann–Liouville and Caputo fractional derivatives are defined as follows [30]:

$$_aD_t^p f(t) = \frac{d^{[p]+1}d}{t^{[p]+1}} \left[_aD_t^{-([p]-p+1)} f(t) \right], \tag{8}$$

$$_a^C D_t^p f(t) = \, _aD_t^{-([p]-p+1)} \left[\frac{d^{[p]+1}}{dt^{[p]+1}} f(t) \right], \tag{9}$$

where $[p]$ denotes the integer part of p and D and c_D represent the Riemann–Liouville and Caputo fractional derivatives, respectively.

The Laplace transform is a very useful tool in the analysis and design of control systems. The Laplace transform is performed by using the Riemann–Liouville's mathematical model as follows [30]:

$$\mathscr{L}\left[D_t^{-\alpha} f(t)\right] = s^{-\alpha} F(s),$$

$$\mathscr{L}\left[D_t^\beta f(t)\right] = s^\beta F(s) - \sum_{k=0}^{n-1} s^k D_t^{\beta-k-1} f(t)|_{t=0}. \tag{10}$$

Eventually, the fractional-order system is established. For a single variable system, the fractional-order transfer function is expressed as follows [31]:

$$G(s) = \frac{N(s)}{D(s)} = \frac{b_n s^{\beta_n} + b_{n-1} s^{\beta_{n-1}} + . + b_1 s_1^\beta + b_0 s^{\beta_0}}{a_n s^{\alpha_n} + a_{n-1} s^{\alpha_{n-1}} + . + a_1 s^{\alpha_1} + a_0 s^{\alpha_0}}$$

$$= \left(\frac{\sum_{i=0}^n b_i s^{\beta_i}}{\sum_{i=0}^n a_i s^{\alpha_i}} \right), \tag{11}$$

where $b_i, a_i, \alpha_i, \beta_i$ denote the real numbers.

Generally, it is not possible to obtain the numerical solution of fraction differential equations based on standard definitions. One intuitive idea to address this problem is to approximate numerical solution by using filters. We assume that the expected fitting range is (ω_b, ω_h). Then, the filter is mathematically expressed as follows [32]:

$$G_f(s) = K \prod_{k=1}^N \frac{s + \omega_k'}{s + \omega_k},$$

$$\omega_k' = \omega_b \left(\frac{\omega_h}{\omega_b} \right)^{[k+N+(1-\gamma)/2]\,(2N+1)}, \omega_k = \omega_b \left(\frac{\omega_h}{\omega_b} \right)^{[k+N+(1+\gamma)/2]/(2N+1)}, K = \omega_h^\gamma. \tag{12}$$

As a most natural generalization of the exponential function, the Mittag–Leffler function is particularly important in fractional-order system analysis. The mathematical definition of the Mittag–Leffler function with three parameters is [31]

$$E_{\alpha,\beta}^\gamma(z) = \sum_{k=0}^\infty \frac{(\gamma)_k}{\Gamma(\alpha k + \beta)} \frac{z^k}{k!}, \tag{13}$$

where $\alpha, \beta, \gamma \in C$, $\mathrm{Re}(\alpha) > 0$, $\mathrm{Re}(\beta) > 0$, $\mathrm{Re}(\gamma) > 0$, and $(\gamma)_k$ is the Pochhammer symbol.

Property 1. (see [30])

$$_aD_t^p \left(_aD_t^q f(t) \right) =$$

$$_aD_t^{p+q} f(t) - \sum_{j=1}^n \left[_aD_t^{q-j} f(t) \right]_{t=a} \frac{(t-a)^{-p-j}}{\Gamma(1-p-j)}. \tag{14}$$

Lemma 1 (see [33]). *We consider the fractional nonautonomous system* $_{t_0}^C D_t^\alpha x(t) = f(t, x)$, *where* $f(t, x)$ *represents the real-valued continuous function, we have*

$$\left\| t_0 D_t^{-\alpha} f(t, x(t)) \right\| \le t_0 D_t^{-\alpha} \| f(t, x(t)) \|, \tag{15}$$

where $\alpha \ge 0$ *and* $\| \cdot \|$ *denotes an arbitrary norm.*

Lemma 2 (see [25]). *Let $x = 0$ be an equilibrium point of the asymptotic stability of the fractional nonautonomous system $_0D_t^\alpha x(t) = f(t, x)$ and $\mathbb{D} \subset \mathbb{R}^n$ be a domain containing the origin. Let $V t, x t)$: $[0, \infty) \times \mathbb{D} \longrightarrow \mathbb{R}$ be a continuously differentiable function and locally Lipschitz with respect to x, such that*

$$\alpha_1 \|x\|^a \le V(t, x(t)) \le \alpha_2 \|x\|^{ab},$$
$$D_t^\beta V(t, x(t)) \le -\alpha_3 \|x\|^{ab}, \tag{16}$$

where $t \ge 0, x \in \mathbb{D}, \beta \in (0, 1), \alpha_1, \alpha_2, \alpha_3, a,$ and b denotes the arbitrary positive constants. Then, $x = 0$ is the Mittag–Leffler stable. If the assumptions hold globally on $\mathbb{R}^n$, then $x = 0$ is globally the Mittag–Leffler stable. In addition, if there exists a constant t_1, the equilibrium point $x = 0$ is generalized Mittag–Leffler stability for $t \ge t_1$.

3.2. Design of the Fractional-Order Active Disturbance Rejection Control.

In this section, the fractional-order active disturbance rejection position control scheme of position control of antenna is presented. ADRC insightfully proposed the integrator chain of the controlled variable as the most fundamental structure for control systems, linear or nonlinear. Moreover, it generalized the concept of disturbance to the "total disturbance." Figure 5 presents the ADRC consists of extended state observer and controller. The function of the extended state observer is to expand the total disturbance into a new state variable of the system and then use the input and output of the system to observe all the states including the original state variables and disturbances in the system. The controller compensates the total disturbance to simplify the plant to a cascade integral form, which can be easily controlled by the tracking error and its derivative. In fact, we can use different linear or nonlinear gain combinations in the ESO and the feedback in the same ADRC structure.

First, the antenna control system is processed using the ADRC framework. The antenna servo control system is a typical form of integrator cascade. Therefore, a fractional-order active disturbance rejection controller for a large antenna is designed based on second-order integrator cascade form. The difference between the transfer function of the antenna and the second-order integrator cascade form can be regarded as the model uncertainty w_1, the wind gust, and friction, and the damping inertial effect from the dish can be considered as the external disturbance w_2. The model uncertainty and unmodeled internal and external disturbances constitute the total disturbance. The total disturbance can be estimated and compensated based on a fractional-order extended state observer, which attenuates the adverse effects caused by the wind.

The antenna control system is mathematically expressed as

$$\ddot{y} = bu + w_1 + w_2. \tag{17}$$

Let b_0 represent the nominal value of b. Due to the inadequacy of differential in stability and response to high
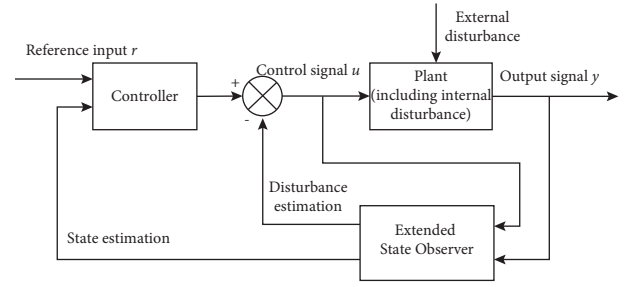

Figure 5: The state-space diagram of ADRC.

frequency noise, a fractional-order differential is introduced to design FOESO. Now, (17) can be rewritten as follows:

$$y^{(2\alpha)} = -\ddot{y} + y^{(2\alpha)} + w_1 + w_2 + (b - b_0)u + b_0 u. \tag{18}$$

We define the total disturbance as $f = -\ddot{y} + w_1 + w_2 + (b - b_0)u$. Then, (18) is further simplified as follows:

$$y^{(2\alpha)} = f + b_0 u. \tag{19}$$

We define

$$\begin{cases} y = \theta_a, \\ x_1 = y, \\ x_2 = y^\alpha, \\ x_3 = f, \end{cases} \tag{20}$$

where x_1 and x_2 denote state variables and x_3 denotes the extended state variable. Let $h = f^\alpha$; then, the following state-space representation is obtained:

$$\begin{cases} x_1^{(\alpha)} = x_2, \\ x_2^{(\alpha)} = x_3 + b_0 u, \\ x_3^{(\alpha)} = h, \\ y = x_1. \end{cases} \tag{21}$$

Now, FOESO is designed by combining the fractional differential and linear ESO. FOESO improves the observation ability and alleviates the contradiction between anti-interference ability and antinoise ability of LESO. The fractional-order extended state observer is constructed as follows:

$$\begin{cases} z_1^{(\alpha)} = \beta_1 (y - z_1) + z_2, \\ z_2^{(\alpha)} = \beta_2 (y - z_1) + z_3 + b_0 u, \\ z_3^{(\alpha)} = \beta_3 (y - z_1), \end{cases} \tag{22}$$

where $\beta_1, \beta_2, \beta_3$ denote the observer gains of FOESO and α denotes the observer order of FOESO, $\alpha \in (0, 1]$.

If the observer gain β_i is configured by using the bandwidth-parameterization method, we have

$$[\beta_1, \beta_2, \beta_3] = [3\omega_o, 3\omega_o^2, \omega_o^3], \omega_o > 0, \tag{23}$$

where ω_o denotes the bandwidth of FOESO.

Finally, with the state observer properly designed, the control law is designed as

$$u = \frac{\left[k_p\left(r - z_1\right) - k_d z_2 - z_3\right]}{b_0}. \tag{24}$$

Using the bandwidth-parameterization method, we obtain

$$\left[k_d, k_p\right] = \left[2\omega_c, \omega_c^2\right], \omega_c > 0, \tag{25}$$

where ω_c denotes the bandwidth of the controller.

In summary, the FOADRC proposed in this study is mainly based on the structure of ADRC by improving the linear ESO to FOESO. The FOADRC controller for large antenna system is shown in Figure 6.

4. Convergence and Frequency-Band Characteristic Analysis of FOESO

The convergence and frequency-band characteristic analysis of FOESO is described in the following sections.

4.1. Convergence of FOESO. In the bandwidth of FOESO, we note that the gain factor is $\kappa_i = 3!/i! \times (3 - i)!, i = 1, 2, 3$, and $\beta_i = \kappa_i/\varepsilon^i$. We obtain the dynamic observation error as follows:

$$\begin{cases} e_1(t) = x_1(t) - z_1(t), \\[2mm] z_1^\alpha(t) = z_2(t) + \dfrac{\kappa_1}{\varepsilon}e_1(t), \\[2mm] z_2^\alpha(t) = z_3(t) + \dfrac{\kappa_2}{\varepsilon^2}e_1(t) + b_0 u(t), \\[2mm] z_3^\alpha(t) = \dfrac{\kappa_3}{\varepsilon^3}e_1(t). \end{cases} \tag{26}$$

With $g_i(e_1(t)) = \alpha_i e_1(t) (i = 1, 2, 3)$, the forementioned system attains a high gain form and is expressed as follows:

$$\begin{cases} e_1(t) = x_1(t) - z_1(t), \\[2mm] z_1^\alpha(t) = z_2(t) + \dfrac{1}{\varepsilon}g_1(e_1(t)), \\[2mm] z_2^\alpha(t) = z_3(t) + \dfrac{1}{\varepsilon^2}g_2(e_1(t)) + b_0 u(t), \\[2mm] z_3^\alpha(t) = \dfrac{1}{\varepsilon^3}g_3(e_1(t)). \end{cases} \tag{27}$$

Assumption 1. There exists a positive constant, such that the α-order derivation of total disturbance f is bounded and satisfies the following condition:

$$\left|\frac{d^\alpha f\left(t, x_1(t), x_2(t), w(t)\right)}{dt^\alpha}\right| \leq M. \tag{28}$$

Assumption 2. There exists a positive constant $\lambda_i (i = 1, 2, 3, 4)$ and a continuous positive definite function $V: R^3 \longrightarrow R$ for unknown function $g_i(\cdot) (i = 1, 2, 3)$, and the following conditions are true as follows:

$$\lambda_1\|x\|^2 \leq V(x) \leq \lambda_2\|x\|^2,$$

$$\frac{\partial V}{\partial x_1}\left(x_2 - g_1(x_1)\right) + \frac{\partial V}{\partial x_2}\left(x_3 - g_2(x_1)\right)$$

$$\frac{\partial V}{\partial x_3}g_3(x_1) \leq -\lambda_3\|x\|, \tag{29}$$

$$\frac{\partial V}{\partial x_3} \leq -\lambda_4\|x\|.$$

Assumption 3. System (27) observational error function for (20) satisfies the Lipschitz condition, and the Lipschitz constant l is positive.

Theorem 1. *If Assumptions 1 and 2 are satisfied, FOESO achieves asymptotic stability.*

Proof. We define system (27) observational error function for (20) as follows:

$$\begin{aligned} e(t) &= \left[x_1(t) - z_1(t), x_2(t) - z_2(t), x_3(t) - z_3(t)\right] \\ &= \left[e_1(t), e_2(t), e_3(t)\right]. \end{aligned} \tag{30}$$

We note

$$\hat{z}_i(t) = \frac{e_i(\varepsilon t)}{\varepsilon^{3-i}}, i = 1, 2, 3. \tag{31}$$

Then, the observation error dynamics of system from (27) to (20) are expressed as follows:

$$\begin{cases} \hat{z}_1^\alpha(t) = \hat{z}_2(t) - g_1\left(\hat{z}_1(t)\right), \\[2mm] \hat{z}_2^\alpha(t) = \hat{z}_3(t) - g_2\left(\hat{z}_1(t)\right), \\[2mm] \hat{z}_3^\alpha(t) = -g_3\left(\hat{z}_1(t)\right) + \varepsilon f^\alpha(t). \end{cases} \tag{32}$$

For simplicity, we note ${}_0^C D_t^\alpha \quad \hat{z}(t) = f^*(t, \hat{z})de$ r derivative of the Lyapunov function $V(\hat{z}(t))$ to the system (32) with respect to time t is expressed as
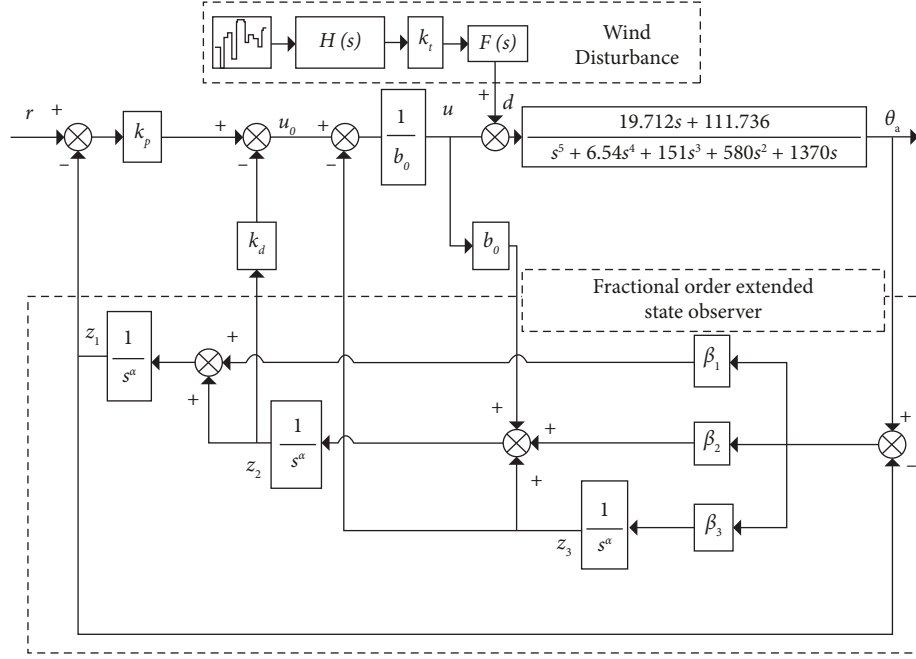
FIGURE 6: The proposed structure of FOADRC for the antenna.

$$\,_{0}^{C}D_{t}^{1-\alpha}V(\hat{z}(t)) = \,_{0}D_{t}^{-\alpha}\dot{V}(\hat{z}(t)),$$

$$= \,_{0}D_{t}^{-\alpha}\left(\frac{\partial V}{\partial x_{1}}(x_{2} - g_{1}(x_{1})) + \frac{\partial V}{\partial x_{2}}(x_{3} - g_{2}(x_{1})),\right.$$

$$\left.-\frac{\partial V}{\partial x_{3}}g_{3}(x_{1}) + \frac{\partial V}{\partial x_{3}}\varepsilon\frac{d^{\alpha}f(t)}{dt^{\alpha}}\right),$$

$$\leq \,_{0}D_{t}^{-\alpha}\left(-\lambda_{3}\|x\| - \lambda_{4}M\|x\|\right),$$

$$= -(\lambda_{3} + \lambda_{4}M)_{0}D_{t}^{-\alpha}\|x\|,$$

$$= -(\lambda_{3} + \lambda_{4}M)l^{-1}\,_{0}D_{t}^{-\alpha}\left\|f^{*}(t,\hat{z})\right\|,$$

$$\leq -(\lambda_{3} + \lambda_{4}M)l^{-1}\left\|\,_{0}D_{t}^{-\alpha}f^{*}(t,\hat{z})\right\|,$$

$$= -(\lambda_{3} + \lambda_{4}M)l^{-1}\|x\|.$$

(33)

Therefore, the conclusion can be obtained by using Lemma 2, i.e., the proposed FOESO is the Mittag–Leffler stable and asymptotic stable.

In summary, based on the assumptions similar to the ESO presented in [34] and generalized Mittag–Leffler stability of fractional-order nonlinear dynamic systems, the dynamic system describing the observation error of the proposed FOESO is asymptotic stable.   □

4.2. Frequency-Band Characteristics Analysis of FOESO.
As the core of FOADRC, the tracking and estimation capacity of FOESO determines the performance of FOADRC. In this section, we present the rejection quality for external disturbance, the difference between FOESO and ESO, and the relations between the dynamic characteristics and the observer parameters.

Based on the Laplace transformation presented in (22) and (23), we have

$$z_{1} = \frac{3\omega_{o}s^{2\alpha} + 3\omega_{o}^{2}s^{\alpha} + \omega_{o}^{3}}{\left(s^{\alpha} + \omega_{o}\right)^{3}}y + \frac{b_{0}s^{\alpha}}{\left(s^{\alpha} + \omega_{o}\right)^{3}}u,$$

$$z_{2} = \frac{\left(3\omega_{o}^{2} + \omega_{o}^{3}\right)s^{\alpha}}{\left(s^{\alpha} + \omega_{o}\right)^{3}}y + \frac{b_{0}\left(s^{\alpha} + 3\omega_{o}\right)s^{\alpha}}{\left(s^{\alpha} + \omega_{o}\right)^{3}}u,$$

$$z_{3} = \frac{\omega_{o}^{3}s^{2\alpha}}{\left(s^{\alpha} + \omega_{o}\right)^{3}}y - \frac{b_{0}\omega_{o}^{3}}{\left(s^{\alpha} + \omega_{o}\right)^{3}}u.$$

(34)

The tracking errors are mathematically expressed as follows:

$$e_1 = z_1 - y = -\frac{s^{3\alpha}}{(\omega_o + s^\alpha)^3} y + \frac{b_0 s^\alpha}{(\omega_o + s^\alpha)^3} u,$$

$$e_2 = z_2 - y^{(\alpha)} =$$

$$-\frac{s^{3\alpha}(3\omega_o + s^\alpha)}{(\omega_o + s^\alpha)^3} y + \frac{b_0 s^\alpha(3\omega_o + s^\alpha)}{(\omega_o + s^\alpha)^3} u, \quad (35)$$

$$e_3 = z_3 - \left(y^{(2\alpha)} - b_0 u\right) = -\frac{s^{3\alpha}\left(3\omega_o s^\alpha + s^{2\alpha} + 3\omega_o^2\right)}{(\omega_o + s^\alpha)^3} y$$

$$+\frac{b_0 s^\alpha\left(3\omega_o s^\alpha + s^{2\alpha} + 3\omega_o^2\right)}{(\omega_o + s^\alpha)^3} u.$$

$$\begin{cases} e_{1s} = \lim_{s \to 0} s e_1 \\[2mm] = \lim_{s \to 0} \dfrac{-Ks^{3\alpha} + Kb_0 s^\alpha}{s^{3\alpha} + 3\omega_o s^{2\alpha} + 3\omega_o s^\alpha + \omega_o^3} = 0 \\[4mm] e_{2s} = \lim_{s \to 0} s e_2 \\[2mm] = \lim_{s \to 0} \dfrac{-Ks^{4\alpha} - 3K\omega_o s^{3\alpha} + Kb_0 s^{2\alpha} + 3Kb_0 \omega_o s^\alpha}{s^{3\alpha} + 3\omega_o s^{2\alpha} + 3\omega_o s^\alpha + \omega_o^3} = 0 \\[4mm] e_{3s} = \lim_{s \to 0} s e_3 \\[2mm] = \lim_{s \to 0} \left(\dfrac{-Ks^{5\alpha} - 3K\omega_o s^{4\alpha} + \left(Kb_0 - 3K\omega_o^2\right)s^{3\alpha}}{s^{3\alpha} + 3\omega_o s^{2\alpha} + 3\omega_o s^\alpha + \omega_o^3} + \dfrac{3Kb_0\omega_o s^{2\alpha} + 3Kb_0\omega_o s^\alpha}{s^{3\alpha} + 3\omega_o s^{2\alpha} + 3\omega_o s^\alpha + \omega_o^3} \right) \\[4mm] = 0 \end{cases} \quad (36)$$

The expression presented in (36) shows that the FOESO achieves unbiased estimation of system state variables and total disturbance.

The analysis of the FOESO's dynamic tracking process is presented. When $b_0 = 0$, the response of z_1 to step signal $y(s) = K/s$ is expressed as follows:

$$z_1 = \frac{3\omega_o s^{2\alpha} + 3\omega_o^2 s^\alpha + \omega_o^3}{(s^\alpha + \omega_o)^3} \frac{K}{s} = 3K\omega_o \frac{s^{2\alpha-1}}{(s^\alpha + \omega_o)^3}$$

$$+ 3K\omega_o^2 \frac{s^{\alpha-1}}{(s^\alpha + \omega_o)^3} + K\omega_o^3 \frac{1}{s(s^\alpha + \omega_o)^3}. \quad (37)$$

Considering the typicality of the analysis, the steady-state errors are obtained by considering the step signal with amplitude K on both y and u as follows:

By inverting the Laplace transformation, we obtain

$$z_1(t) = 3K\omega_o\left[t^\alpha E^3_{(\alpha,\alpha+1)}\left(-\omega_o t^\alpha\right)\right]$$

$$+3K\omega_o^2\left[t^{2\alpha} E^3_{(\alpha,2\alpha+1)}\left(-\omega_o t^\alpha\right)\right] \quad (38)$$

$$+K\omega_o^3\left[(1 - E_\alpha(-\omega_o t^\alpha))t^{2\alpha-1} E^2_{(\alpha,2\alpha)}\left(-\omega_o t^\alpha\right)\right].$$

In this case, integer-order ESO's response in time domain is as follows:

$$z_1(t) = K - K\left(\frac{1}{2}\omega_o^2 t^2 - 2\omega_o t + 1\right)e^{-\omega_o t}. \quad (39)$$

The extreme point of (39) is expressed as follows:

$$z_1(t_1) = K(\sqrt{3} - 1)e^{\sqrt{3}-3} + K \approx 1.206K. \qquad (40)$$

(40) shows that no matter how the bandwidth parameter is chosen, there is always about 20% overshoot during the tracing process in integer-order ESO as presented in Figure 7.

Considering FOESO, theoretically, it is difficult to solve (38) for extreme values; however, the numerical results show that the order of FOESO is related to the overshoot during the tracing process, which can be reduced by decreasing the order of differentiation as presented in Figure 8.

The relationship between FOESO's suppression of external disturbances, noise transfer characteristics, and parameters is discussed. First, the effect of noise δ_o from y is analyzed. From (25), we obtain

$$\frac{z_1}{\delta_o} = \frac{3\omega_o s^{2\alpha} + 3\omega_o^2 s^{\alpha} + \omega_o^3}{(s^{\alpha} + \omega_o)^3}. \qquad (41)$$

When $\alpha = 0.8$ (fixed) and $\omega_o = 5, 10, 15, 20, 25$ are considered for obtaining the Bode diagram as shown in Figure 9, the response speed of the system increases with an increase in ω_o. However, the noise amplification becomes more obvious due to the increase in the high frequency band gain.

When $\omega_o = 10$ (fixed) and $\alpha = 0.6, 0.7, 0.8, 0.9, 1$ are considered for obtaining the Bode diagram as shown in Figure 10, the response speed of the system increases, the gain of the high frequency band decreases, and the noise amplification effect decreases as α decreases.

Second, the effect of input disturbance δ_c from u is analyzed. From (25), we obtain

$$\frac{z_1}{\delta_c} = \frac{b_0 s^{\alpha}}{(s^{\alpha} + \omega_o)^3}. \qquad (42)$$

When $\alpha = 0.8, b_0 = 10$ (fixed) and $\omega_o = 10, 20, ..., 50$ are considered for obtaining the Bode diagram as shown in Figure 11, the phase lag of the tracking signal decreases, while the gain of the high frequency band is not affected at all with an increase in ω_o. Please note that the proposed FOESO has good suppressive ability to input disturbance.

When $\omega_o = 10, b_0 = 10$ (fixed), and $\alpha = 0.6, 0.7, 0.8, 0.9, 1$ are considered for obtaining the Bode diagram as shown in Figure 12, the phase lag of the tracking signal decreases and the high frequency band gain decreases with a decrease in α.

5. Stability Analysis

The stability analysis is described in the following sections.

5.1. Stability of the FOADRC.
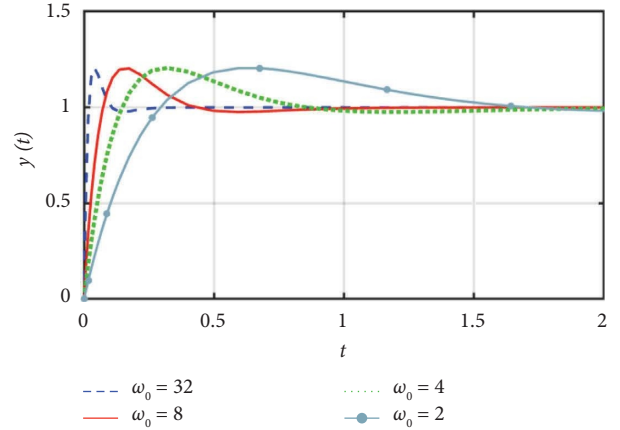By substituting (24) into (22), we obtain

Figure 7: The response of z_1 corresponding to the step signal (ESO).
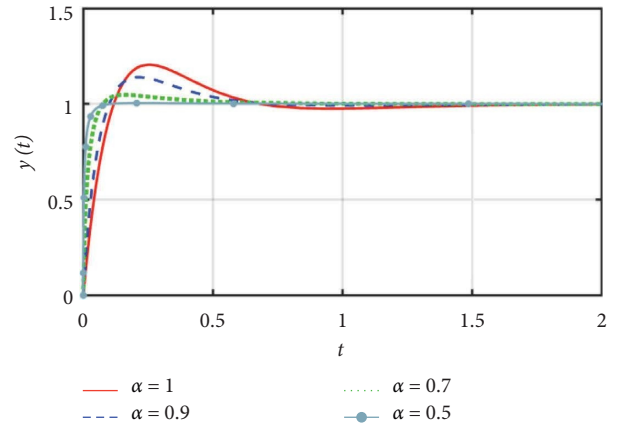

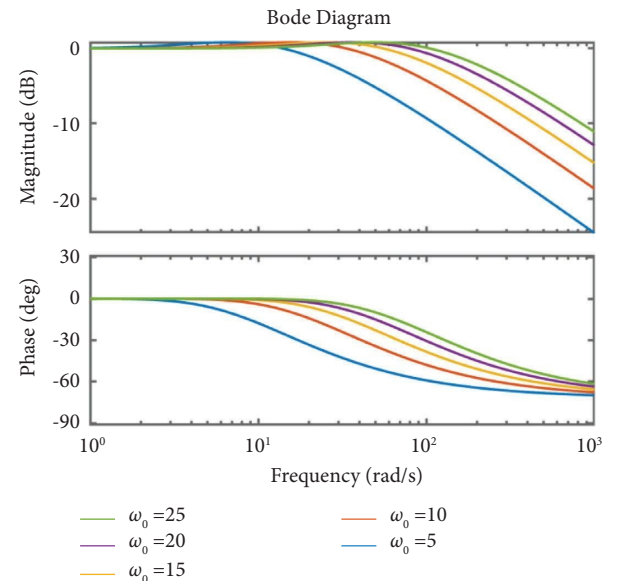Figure 8: The response of z_1 corresponding to step signal (FOESO).

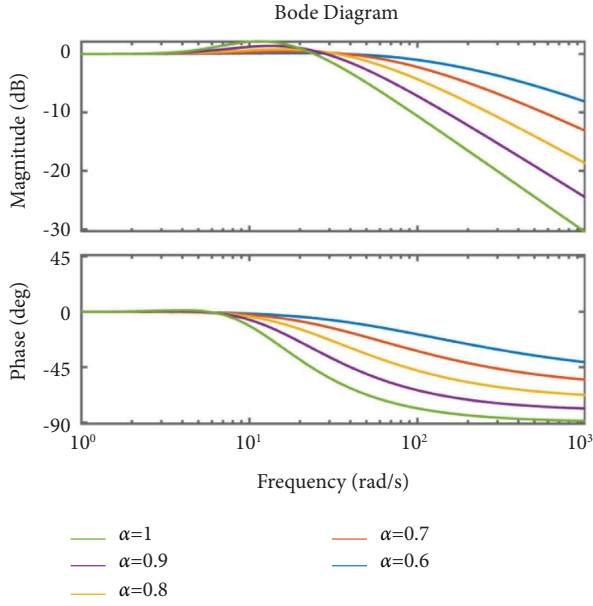Figure 9: The frequency-domain characteristic of FOESO observation noise (observer gain ω_o).

Bode Diagram

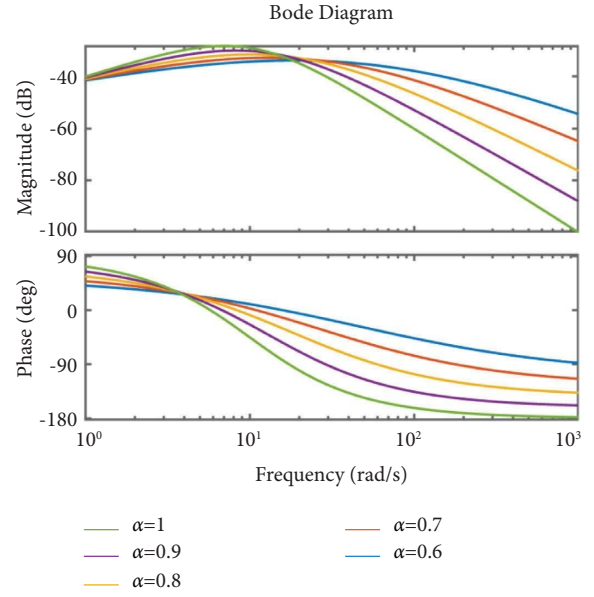FIGURE 10: The frequency-domain characteristic of FOESO observation noise (observer order α).

Bode Diagram

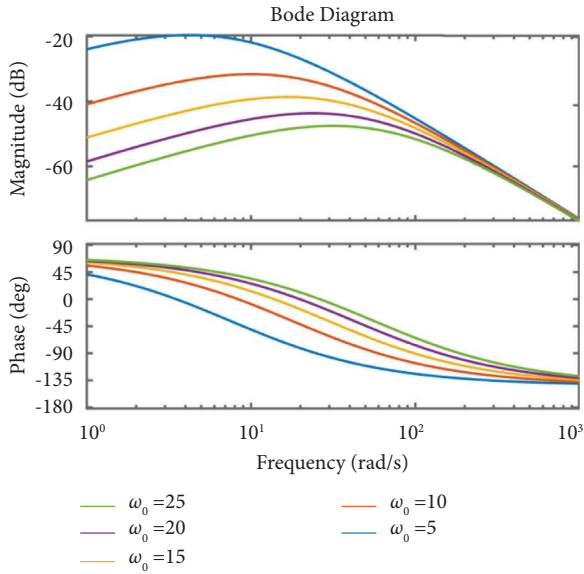FIGURE 11: The frequency-domain characteristic of FOESO input disturbance (observer gain ω_o).

Bode Diagram

FIGURE 12: The frequency-domain characteristic of FOESO input disturbance (observer order α).

$$\begin{bmatrix} z_1^{(\alpha)} \\ z_2^{(\alpha)} \\ z_3^{(\alpha)} \end{bmatrix} = A \begin{bmatrix} z_1 \\ z_2 \\ z_3 \end{bmatrix} + B \begin{bmatrix} r \\ y \end{bmatrix},$$

$$A = \begin{bmatrix} -\beta_1 & 1 & 0 \\ -(\beta_2 + k_p) & -k_d & 0 \\ -\beta_3 & 0 & 0 \end{bmatrix}, B = \begin{bmatrix} 0 & \beta_1 \\ k_p & \beta_2 \\ 0 & \beta_3 \end{bmatrix}. \tag{44}$$

The output matrices of the system are expressed as follows:

$$u = C \begin{bmatrix} z_1 \\ z_2 \\ z_3 \end{bmatrix} + D \begin{bmatrix} r \\ y \end{bmatrix},$$

$$C = \begin{bmatrix} -\dfrac{k_p}{b_0} & -\dfrac{k_d}{b_0} & -\dfrac{1}{b_0} \end{bmatrix}, D = \begin{bmatrix} \dfrac{k_p}{b_0} & 0 \end{bmatrix}. \tag{45}$$

The state-space model of the system is transformed by the inverse Laplace transform, i.e., $G = C(s^\alpha I - A)^{-1} B + D$. The transfer functions from y and r to u are expressed as follows:

$$\frac{U(s)}{Y(s)} = -\frac{\left(\beta_1 k_p + \beta_2 k_d + \beta_3\right)s^{2\alpha} + \left(\beta_2 k_p + \beta_3 k_d\right)s^\alpha + \beta_3 k_p}{b_0 s^\alpha \left[s^{2\alpha} + (\beta_1 + k_d)s^\alpha + \beta_1 k_d + \beta_2 + k_p\right]},$$

$$C_1(s) = \frac{k_p\left(s^{3\alpha} + \beta_1 s^{2\alpha} + \beta_2 s^\alpha + \beta_3\right)}{\left(\beta_1 k_p + \beta_2 k_d + \beta_3\right)s^{2\alpha} + \left(\beta_2 k_p + \beta_3 k_d\right)s^\alpha + \beta_3 k_p},$$

$$\tag{46}$$

Thus, we obtain a block diagram of second-order FOADRC, as shown in Figure 13.

We consider (43) and (24) as a double-input-single-output system with two inputs y and r an output u. Then, the state matrices of the system are defined as follows:

$$\begin{cases} z_1^{(\alpha)} = -\beta_1 z_1 + z_2 + \beta_1 y, \\ z_2^{(\alpha)} = -(\beta_2 + k_p)z_1 - k_d z_2 + \beta_2 y + k_p r, \\ z_3^{(\alpha)} = -\beta_3 z_1 + \beta_3 y. \end{cases} \tag{43}$$

The fractional-order feedback compensator is

$$C(s) = \frac{\left(\beta_1 k_p + \beta_2 k_d + \beta_3\right)s^{2\alpha} + \left(\beta_2 k_p + \beta_3 k_d\right)s^{\alpha} + \beta_3 k_p}{b_0 s^{\alpha}\left[s^{2\alpha} + (\beta_1 + k_d)s^{\alpha} + \beta_1 k_d + \beta_2 + k_p\right]}. \tag{47}$$

The fractional-order prefilter is

$$C_1(s) = \frac{k_p\left(s^{3\alpha} + \beta_1 s^{2\alpha} + \beta_2 s^{\alpha} + \beta_3\right)}{\left(\beta_1 k_p + \beta_2 k_d + \beta_3\right)s^{2\alpha} + \left(\beta_2 k_p + \beta_3 k_d\right)s^{\alpha} + \beta_3 k_p}. \tag{48}$$

The plant is

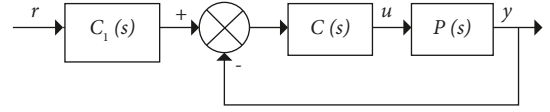$$P(s) = \frac{\sum_{i=0}^{m} m_i s^{m-i}}{\sum_{j=0}^{n} n_j s^{n-j}}. \tag{49}$$

FIGURE 13: The block diagram of second-order FOADRC.

The characteristic equation of the closed-loop system is expressed as follows:

$$1 + C(s)P(s) = 0. \tag{50}$$

Substituting (47) and (49) in (50), we obtain

$$1 + \frac{\left(\beta_1 k_p + \beta_2 k_d + \beta_3\right)s^{2\alpha} + \left(\beta_2 k_p + \beta_3 k_d\right)s^{\alpha} + \beta_3 k_p}{b_0 s^{\alpha}\left[s^{2\alpha} + (\beta_1 + k_d)s^{\alpha} + \beta_1 k_d + \beta_2 + k_p\right]} \times \frac{\sum_{i=0}^{m} m_i s^{m-i}}{\sum_{j=0}^{n} n_j s^{n-j}} = 0. \tag{51}$$

Simplifying (51), we obtain as follows:

$$\begin{aligned}
b_0 s^{\alpha}&\left[s^{2\alpha} + (\beta_1 + k_d)s^{\alpha} + \beta_1 k_d \right.\\
&\left.+ \beta_2 + k_p\right) \times \sum_{j=0}^{n} n_j s^{n-j}\\
&+ \left[\left(\beta_1 k_p + \beta_2 k_d + \beta_3\right)s^{2\alpha} + \left(\beta_2 k_p + \beta_3 k_d\right)s^{\alpha}\right.\\
&\left.+ \beta_3 k_p\right] \times \sum_{i=0}^{m} m_i s^{m-i} = 0.
\end{aligned} \tag{52}$$

Substituting (23) and (25) in (52), we obtain

$$\begin{aligned}
b_0 s^{\alpha}&\left[s^{2\alpha} + (3\omega_o + 2\omega_c)s^{\alpha} + 6\omega_o\omega_c + 3\omega_o^2 + \omega_c^2\right]\\
&\qquad\qquad\qquad\qquad \times \sum_{j=0}^{n} n_j s^{n-j}\\
&+ \left[\left(3\omega_o\omega_c^2 + 6\omega_o^2\omega_c + \omega_o^3\right)s^{2\alpha} + \left(3\omega_o^2\omega_c + 2\omega_o^3\omega_c\right)s^{\alpha}\right.\\
&\left.+ \omega_o^3\omega_c^2\right] \sum_{i=0}^{m} m_i s^{m-i} = 0.
\end{aligned} \tag{53}$$

As long as the parameters $b_0, \omega_c, \omega_o, \alpha$ are selected in such a way that the root of (53) lies in the left half plane of the complex plane, the closed-loop system is BIBO stable.

In summary, the conditions that the parameters should meet the BIBO stability of the closed-loop system are given by equivalent transformation of FOADRC and calculation of the characteristic equation of the closed-loop system.

5.2. The Calculation Method of Stability Region for FOADRC. In this section, in order to improve the tuning efficiency of FOADRC, a method for calculating the stability regions based on D-partition is proposed, and the effectiveness of the proposed calculation method is verified.

Substituting $s = j\omega$ in (53), the boundaries of the stability domain are described by $\omega = 0, \omega = \pm\infty$ and $\omega \in (0, -\infty) \cup (0, +\infty)$, named as real root boundary, infinite root boundary, and complex root boundary, respectively.

(1) $\omega = 0$, the real root boundary D_0 is expressed as follows:

$$\omega_o^3 \omega_c^2 m_m = 0, \tag{54}$$

where $m_m \neq 0$ and $\omega_o > 0$, so D_0 is $\omega_c = 0$.

(2) $\omega = \pm\infty$: the infinite root boundary D_∞ is

$$b_0 n_0 = 0. \tag{55}$$

As b_0 is the estimated value of the high-frequency gain of the plant, $b_0 \neq 0$. There are no relevant parameters in the equation, so this condition is invalid and ignored.

(3) $\omega \in (0, -\infty) \cup (0, +\infty)$: the complex root boundary D_ω is

$$\begin{aligned}
b_0 (j\omega)^{\alpha}&\left[(j\omega)^{2\alpha} + (\beta_1 + k_d)(j\omega)^{\alpha}\right.\\
&\left.+ \beta_1 k_d + \beta_2 + k_p\right] \sum_{j=0}^{n} n_j (j\omega)^{n-j}\\
&+ \left[\left(\beta_1 k_p + \beta_2 k_d + \beta_3\right)(j\omega)^{2\alpha}\right.\\
&\left.+ \left(\beta_2 k_p + \beta_3 k_d\right)(j\omega)^{\alpha}\right.\\
&\left.+ \beta_3 k_p \sum_{i=0}^{m} m_i (j\omega)^{m-i} = 0.\right.
\end{aligned} \tag{56}$$

The noninteger power of a complex number $(\sigma + j\omega)^{\gamma}$ is calculated as follows:

$$(\sigma + j\omega)^{\gamma} = \sqrt[\gamma]{\sigma^2 + \omega^2}\left[\cos\left(\gamma \tan^{-1}\frac{\omega}{\sigma}\right) + j\sin\left(\gamma \tan^{-1}\frac{\omega}{\sigma}\right)\right]. \tag{57}$$

Based on the above equation, we obtain

$$j^{2\alpha} = \cos(\pi\alpha) + j\sin(\pi\alpha),$$

$$j^{\alpha} = \cos\left(\frac{\pi}{2}\alpha\right) + j\sin\left(\frac{\pi}{2}\alpha\right). \tag{58}$$

Substituting (58) in (56) and simply replaced with real part and imaginary part, we can rewrite it as follows:

$$1 + (a_c(\omega) + jb_c(\omega))(a(\omega) + jb(\omega)) = 0. \tag{59}$$

The real and imaginary parts are determined as follows:

$$\begin{cases} G_p(j\omega) = r(\omega)e^{i\vartheta(\omega)} = a(\omega) + jb(\omega), \\ G_c(j\omega) = r_c(\omega)e^{i\vartheta(\omega)} = a_c(\omega) + jb_c(\omega), \end{cases} \tag{60}$$

where G_p and G_c, respectively, represent the frequency-domain response of the controlled plant and the feedback controller of FOADRC.

Let the real and imaginary parts be zero, respectively, and the following conditions are obtained:

$$\begin{cases} 1 + a(\omega)a_c(\omega) - b(\omega)b_c(\omega) = 0, \\ a(\omega)b_c(\omega) + a_c(\omega)b(\omega) = 0. \end{cases} \tag{61}$$

Based on the analysis of the above three boundaries and the preset conditions, the stability region boundary of FOADRC is expressed as follows:

$$\begin{cases} D_0: \omega_c = 0, \\ D_\omega: \begin{cases} 1 + a(\omega)a_c(\omega) - b(\omega)b_c(\omega) = 0, \\ a(\omega)b_c(\omega) + a_c(\omega)b(\omega) = 0, \end{cases} \\ \omega_o = 0. \end{cases} \tag{62}$$

Using this computation method for antenna (2), the stability region for FOADRC controller of the antenna is as follows:

$$\begin{cases} a(\omega) = \dfrac{2\left(123200\omega^4 - 14035991\omega^2 - 236259000\right)}{5\left(2500\omega^8 - 648071\omega^6 + 44886500\omega^4 - 193350000\omega^2 + 4692250000\right)}, \\[3mm] b(\omega) = \dfrac{4\left(53689\omega^4 + 16997425\omega^2 - 478369750\right)}{5\omega\left(2500\omega^8 - 648071\omega^6 + 44886500\omega^4 - 193350000\omega^2 + 4692250000\right)}, \\[3mm] a_c(\omega) = \dfrac{\omega_o\left(6\omega_c\omega_o + \omega^{2\alpha}\left(2\sigma_5^{\;2} - 1\right) + \omega_c^2 + 3\omega_o^2 + \sigma_3\right)\left(\sigma_5\omega_c^2\omega_o^2 + 3\omega^\alpha\omega_c^2\omega_o + 3\omega^{2\alpha}\sigma_5\omega_c^2 + 2\omega^\alpha\omega_c\omega_o^2 + 6\omega^{2\alpha}\sigma_5\omega_c\omega_o + \omega^{2\alpha}\sigma_5\omega_o^2\right)}{\sigma_1} \\[2mm] \quad + \dfrac{\omega_o\sigma_4\sigma_2\left(-\omega_c^2\omega_o^2 + 3\omega^{2\alpha}\omega_c^2 + 6\;\;\omega^{2\alpha}\omega_c\omega_o + \omega^{2\alpha}\omega_o^2\right)}{\sigma_1}, \\[3mm] b_c(\omega) = \dfrac{\omega_o\sigma_4\left(-\omega_c^2\omega_o^2 + 3\omega^{2\alpha}\omega_c^2 + 6\omega^{2\alpha}\omega_c\omega_o + \omega^{2\alpha}\omega_o^2\right)\left(6\omega_c\omega_o + \omega^{2\alpha}\left(2\sigma_5^{\;2} - 1\right) + \omega_c^2 + 3\omega_o^2 + \sigma_3\right)}{\sigma_1} \\[2mm] \quad + \dfrac{\omega_o\sigma_2\left(\sigma_5\omega_c^2\omega_o^2 + 3\omega^\alpha\omega_c^2 wo + 3\omega^{2\alpha}\sigma_5\omega_c^2 + 2\omega^\alpha\omega_c\omega_o^2 + 6\omega^{2\alpha}\sigma_5\omega_c\omega_o + \omega^{2\alpha}\sigma_5\omega_o^2\right)}{\sigma_1}, \\[3mm] \sigma_1 = b_0\omega^\alpha\left(\left(\omega^{2\alpha}\cos(\pi\alpha) + 6\omega_c\omega_o + \omega_c^2 + 3\omega_o^2 + \sigma_3\right)^2 + \sigma_2^{\;2}\right), \\[3mm] \sigma_2 = \omega^{2\alpha}\sin(\pi\alpha) + 2\omega^\alpha\omega_c\sigma_4 + 3\omega^\alpha\omega_o\sigma_4, \\[3mm] \sigma_3 = \omega^\alpha\sigma_5\left(2\omega_c + 3\omega_o\right), \\[3mm] \sigma_4 = \sin\left(\dfrac{\pi\alpha}{2}\right), \\[3mm] \sigma_5 = \cos\left(\dfrac{\pi\alpha}{2}\right). \end{cases} \tag{63}$$

$1/b_0 = 1.667$ and we solve (61) and (62) for each ω to obtain the stability region as presented in Figures 14 and 15; it is evident that FOADRC has a larger stability region than ADRC ($\alpha = 1$).

In order to verify the boundary of the stability region, we consider step signal as the input, and $\alpha = 0.9$ and $\omega_c = 6.053$. The simulation results of $w_o = 7, 10, 14,$ and 17 cases are obtained. Figure 16 shows the accuracy of the boundary of the stability domain.

6. Simulation Results

In this section, we evaluate the proposed FOADRC control scheme by performing simulations in MATLAB. The transfer function of the antenna plant and the method to simulate the wind disturbance are presented in Section 2. The parameters of FOADRC are $\omega_o = 5, \omega_c = 8.05,$ and $\alpha = 0.9$, the parameters of ADRC are $\omega_o = 5$ and $\omega_c = 8.05$, and the parameters of PI are $k_p = 13.1071$ and $k_i = 8.0575$. The performance of FOADRC is mainly evaluated based on the response towards a step signal, response to a sinusoidal signal, doubling of disturbance, and parameters' perturbation. Please note that the simulation time is 20 s. In addition to the overshoot and adjustment time, the error integral criteria are also considered to measure the size of system errors. The integral square error (ISE), integral time squared error (ITSE), integral absolute error (IAE), and integral time absolute error (ITAE) are computed by using the following expressions:

$$\begin{aligned} \text{ISE} &= \int_0^\infty [e(t)]^2 dt, \\ \text{ITSE} &= \int_0^\infty [e(t)] dt, \\ \text{IAE} &= \int_0^\infty |e(t)| dt, \\ \text{ITAE} &= \int_0^\infty t|e(t)| dt. \end{aligned} \quad (64)$$

6.1. Tracking Performance Analysis. Considering that the input is a step signal with an amplitude of 3 mdeg and start time of 0, the response curves of PI, ADRC, and FOADRC are presented in Figure 17. It is evident that ADRC and FOADRC have a significantly less overshoot than the PI controller, and FOADRC achieves a smaller adjustment time as compared to ADRC. The detailed results are presented in Tables 1 and 2. From Table 1, it is evident that, as compared with the PI controller, the FOADRC reduces overshoot by 38.2%, adjustment time of 2% error band calculation by 30%, and adjustment time of 5% error band calculation by 50.2%. As compared with ADRC, the FOADRC overshoots are nearly identical, but the adjustment time of 2% error band calculation is reduced by 22% and that of 5% error band calculation is reduced by 25.3%.

Table 2 presents the four error integral criteria which show that the error in the response of FOADRC to step signals is much smaller as compared to the PI controller used in antenna and also smaller as compared to ADRC. As
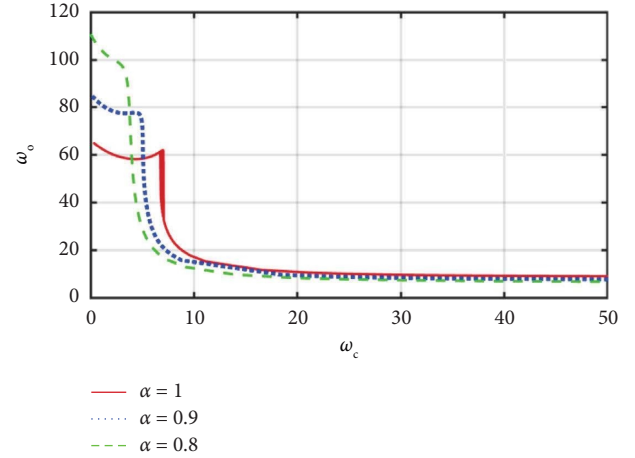

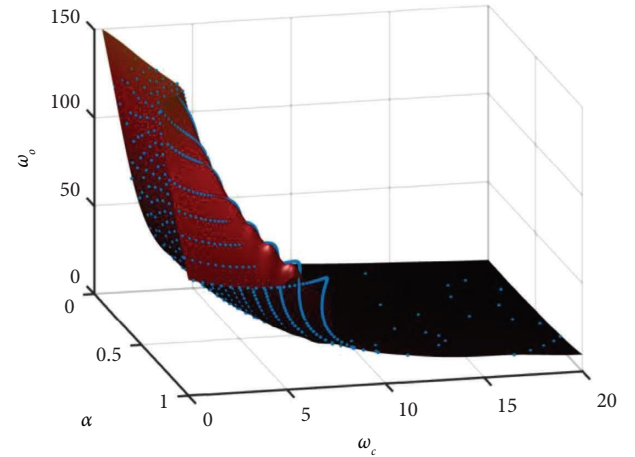FIGURE 14: The stability region of the antenna (ω_c, ω_o).

FIGURE 15: The stability region of the antenna ($\omega_c, \alpha, \omega_o$).
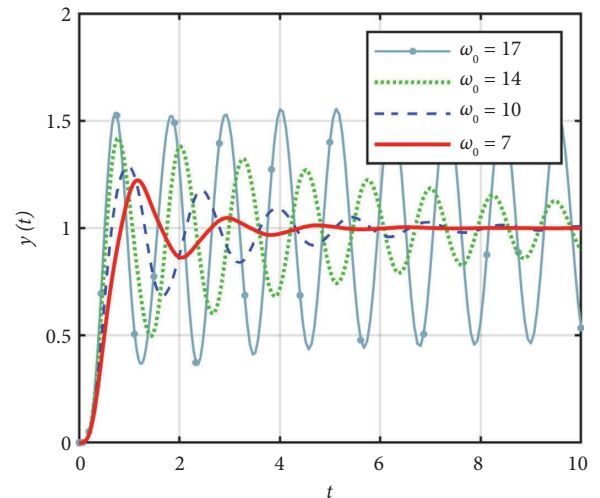

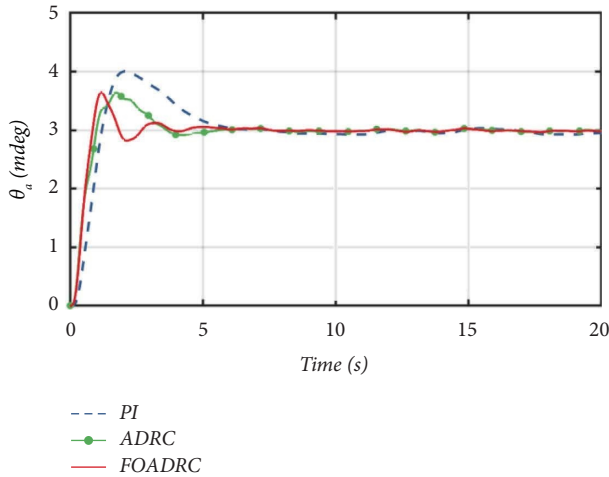FIGURE 16: The step response for the FOADRC.

FIGURE 17: The step responses for three controllers.

TABLE 1: The dynamic performance of three controllers.

Controllers	Overshoot (%)	Adjustment time (s)	
		2% error band	5% error band
PI	34.8	5.14	4.7308
ADRC	21.35	4.65146	3.1587
FOADRC	21.49	3.5990	2.3581

TABLE 2: The error integral criteria of three controllers.

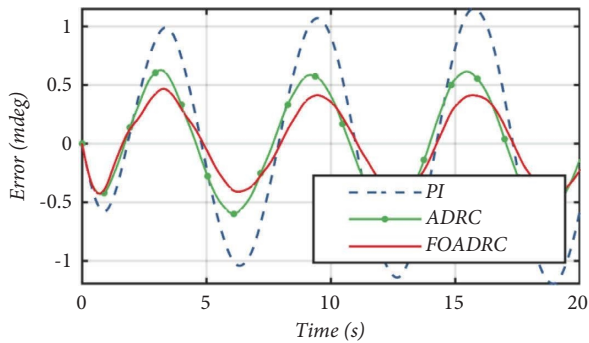| Controllers	ISE	ITSE	IAE	ITAE
PI	6.943	6.696	5.159	15.19
ADRC	3.847	1.703	2.8	5.543
FOADRC	3.624	1.105	2.312	4.419

FIGURE 18: The error curve of sine input for three controllers.

compared with the PI controller, the ISE index decreased by 47.8%, ITSE index decreased by 83.5%, IAE index decreased by 55.19%, and ITAE index decreased by 70.91%.

Figure 18 shows the error curves corresponding to the three controllers when the sinusoidal signal with amplitude of 1 mdeg and frequency of 1 rad/sec is used as an input. The proposed FOADRC traces the sinusoidal signal much better as compared to the PI controller and slightly better as compared to the ADRC.
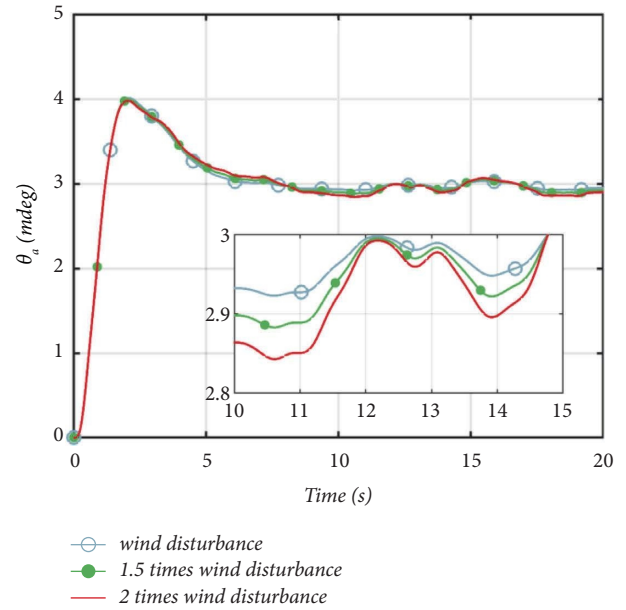

FIGURE 19: The step response of the PI controller when wind disturbance is increased.
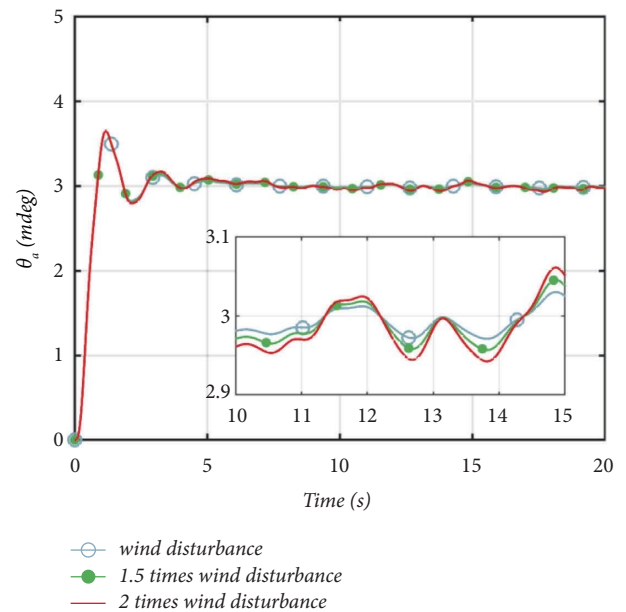

FIGURE 20: The step response of the ADRC controller when wind disturbance is increased.

6.2. Robustness Analysis. In order to verify the performance of the controller in wind disturbance and model uncertainty, the simulation is performed by increasing the wind disturbance by factors of 1.5 and 2. Figure 19 presents the simulation results of the PI controller under three wind disturbances. Figure 20 shows the simulation results of the proposed FOADRC under three wind disturbances. Please note that the response of the two controllers does not deteriorate in dynamic adjustment. However, when the steady

TABLE 3: The dynamic performance of three controllers (double wind disturbance).

Controllers	Overshoot (%)	Adjustment time (s)	
		2% error band	5% error band
PI	32.6	15.6407	10.86
ADRC	21.11	14.9044	3.28
FOADRC	21.54	14.8981	3.41

TABLE 4: The error integral criteria of three controllers (double wind disturbance).

Controllers	ISE	ITSE	IAE	ITAE
PI	7.057	8.154	5.877	23.5
ADRC	3.845	1.831	2.985	8.069
FOADRC	3.65	1.308	2.597	7.348

- ─✱─ *Permeter perturbation* (−10%)
- ─●─ *Permeter perturbation* (−20%)
- ─○─ *Permeter perturbation* (+10%)
- ─▽─ *Permeter perturbation* (+20%)
- ─◇─ *Original response*
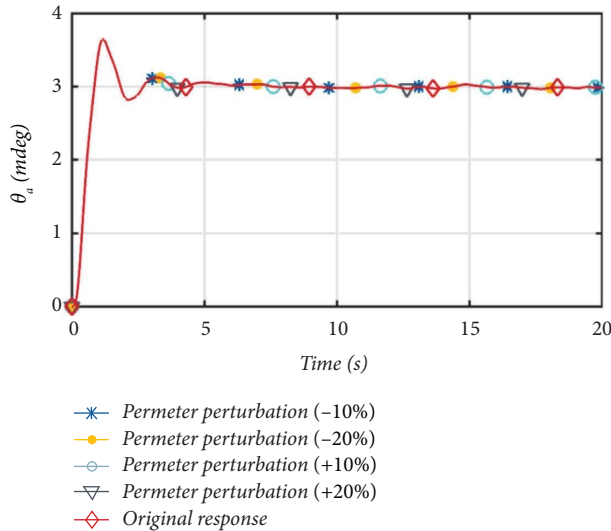
FIGURE 21: The step response of the ADRC controller when parameters are perturbed (±10% and ±20%).

state is reached, it can be seen from the local magnification diagram that the performance deterioration of FOADRC after increasing wind disturbance is significantly less as compared to the PI controller.

The dynamic performance indicators in the case of double wind disturbance are shown in Table 3. As compared with Table 1, it can be seen that the overshoot of the three controllers hardly changes when the wind disturbance is increased by 2 times, but the adjustment time of the PI controller increases by 2–3 times. The time consumed by the proposed FOADRC to enter the 2% error band increases, but the process for entering the 5% error band is still fast.

The error integral criteria for the case where the wind disturbance is doubled are shown in Table 4. The four error integral criteria for FOADRC are still less than ADRC and PI controller. As compared with the PI controller, the FOADRC decreased by 48.28% under ISE criteria, 83.96% under ITSE criteria, 55.81% under IAE criteria, and 68.73% under ITAE criteria.

The step response curves of FOADRC with parameter perturbations of the antenna transfer function model are shown in Figure 21. The response curves of the four parameter perturbations overlap the original response curves completely, indicating that the FOADRC performs well in response to parameter perturbations.

7. Conclusions

The wind disturbance is the primary factor that affects the accuracy of large radio telescope antennas. In this study, a fractional-order active disturbance rejection controller is designed and applied to an antenna based on the existing system configuration. A fractional-order extended state observer is used to estimate the parameter uncertainties, various feedback disturbances, and wind disturbances as a total disturbance. The stability, the disturbance rejection quality, and noise sensitivity characteristic are fully analyzed. The simulation results show that the FOADRC improves the control system capability of resistance to wind disturbance and limits the response overshoot (from 34.8% to 21.49%) and coverages faster compared to other industrial controller (from 5.14 to 3.599). The fractional-order integration contains an additional weight function, and the initial stage has a larger integral response value, so the FOESO can be estimated the state more quickly and accurately, and ultimately FOADRC can achieve better control performance.

Data Availability

The data used to support the findings of this study are included within the article.

Conflicts of Interest

The authors declare that they have no conflicts of interest.

References

[1] R. M. Prestage and R. J. Maddalena, "The Green Bank Telescope: current status and early results," *Proceedings of SPIE*, vol. 4837, pp. 944–953, 2003.

[2] N. Wang, "Xinjiang Qitai 110 m radio telescope," *Sci Sin-Phys Mech Astron*, vol. 44, no. 8, pp. 783–794, 2014, (in Chinese).

[3] J. Zhang, J. Huang, L. Qiu, and R. Song, "Analysis of reflector vibration-induced pointing errors for large antennas subject to wind disturbance: evaluating the pointing error caused by reflector deformation," *IEEE Antennas and Propagation Magazine*, vol. 57, no. 6, pp. 46–61, 2015.

[4] J. Zhang, J. Huang, P. Zhao, W. Liang, and C. Wang, "Antenna control systems for flexible structure under a wind load," *Proceedings of the Institution of Mechanical Engineers - Part C: Journal of Mechanical Engineering Science*, vol. 233, no. 9, pp. 3050–3059, 2018.

[5] M. Meeks and J Ruze, "Evaluation of the haystack antenna and radome," *IEEE Transactions on Antennas and Propagation*, vol. 6, pp. 723–728, 1971.

[6] H. J. Kaercher and J. W. M. Baars, "Design of the <title>-Design of the Large Millimeter Telescope/Gran Telescopio Millimetrico (LMT/GTM)</title>arge millimeter telescope/gran telescopio millimetrico (LMT/GTM)," *SPIE Proceedings*, vol. 4015, 2000.

[7] D. Bock, "The Australia Telescope National Facility," in *Proceedings of the 2019 URSI Asia-Pacific Radio Science Conference (AP-RASC)*, New Delhi, India, March 2019.

[8] W. Gawronski, "Modeling wind-gust disturbances for the analysis of antenna pointing accuracy," *IEEE Antennas and Propagation Magazine*, vol. 46, pp. 50–58, 2004.

[9] W. . Gawronski, "Servo-performance parameters of the NASA deep space network antennas," *IEEE Antennas and Propagation Magazine*, vol. 49, no. 6, pp. 40–46, 2007.

[10] W. Gawronski, "Antenna Linear-Quadratic-Gaussian (LQG) Controllers: Properties, Limits of Performance, and Tuning Procedure," *Interplanetary Network Progress Report*, vol. 42, pp. 1–18, 2004.

[11] W. K. Gawronski, C. S. Racho, and J. A. Mellstrom, "Application of the LQG and feedforward controllers to the deep space network antennas," *IEEE Transactions on Control Systems Technology*, vol. 4, pp. 417–421, 1995.

[12] L. Yu-Xuan, C. P. Huang, and L. I. Hong-An, "LQG Optimal Controller Design with Wind Disturbance Resistance for Large Antenna of Deep Space Station," *Radio Engineering*, 2012.

[13] G. He, G Li, M Liu, and Y Huang, "LQG controller with wind gust disturbance rejection property for cassegrain antenna," in *Proceedings of the IEEE International Conference on Intelligent Computing & Intelligent Systems*, Shanghai, November 2009.

[14] W. Gawronski, "Antenna control systems: from PI to H/sub/ spl infin//," *IEEE Antennas and Propagation Magazine*, vol. 1, pp. 52–60, 2001.

[15] J. Han, "Active Disturbance Rejection Controller and its Application," *Control and Decision*, p. 01, 1998 (in Chinese).

[16] Y. Huang and W. Xue, "Active Disturbance Rejection Control: Methodology and Theoretical Analysis," *ISA Transactions*, vol. 53, no. 4, pp. 963–976, 2014.

[17] Z. Gao, "Scaling and Bandwidth-Parameterization Based Controller Tuning," in *Proceedings of the 2003 American Control Conference*, IEEE IEEE, Denver, CO, USA, June 2003.

[18] D. Qiu, M. Sun, Z. Wang, Y. Wang, and Z. Chen, "Practical wind-disturbance rejection for large deep space observatory antenna," *IEEE Transactions on Control Systems Technology*, vol. 22, pp. 1983–1990, 2014.

[19] D. Yuan, M. XJ, Q. H. Zeng, and X. Qiu, "Research on Frequency-Band Characteristics and Parameters Configuration of Linear Active Disturbance Rejection Control for Second-Order Systems," *Control Theory & Applications*, vol. 30, no. (12), 2013.

[20] Z. Wu, H. Ting, L. Donghai, and X. Yali, "The Calculation of Stability and Robustness Regions for Active Disturbance Rejection Controller and its Engineering Application," *ADRC & robustness & boiler control*, 2019.

[21] I. Podlubny, "Fractional-order systems and fractional-order controllers," *Conference Internationale Francophone Dautomatique*, 1994.

[22] P. Shah and S. Agashe, "Review of fractional PID controller," *Mechatronics*, vol. 38, pp. 29–41, 2016.

[23] I. Petras, "Stability of Fractional-Order Systems with Rational Orders," arXiv preprint arXiv:081141022008.

[24] S. E. Hamamci, "An algorithm for stabilization of fractional-order time delay systems using fractional-order PID controllers," *IEEE Transactions on Automatic Control*, vol. 52, no. 10, pp. 1964–1969, Oct, 2007.

[25] Y. Li, Y. Q. Chen, and I. Podlubny, "Stability of fractional-order nonlinear dynamic systems: Lyapunov direct method and generalized Mittag–Leffler stability," *Computers & Mathematics with Applications*, vol. 59, no. 5, pp. 1810–1821, 2010.

[26] P. C. Chen, Y. Luo, W. Zheng, Z. Gao, and Y. Chen, "Fractional order active disturbance rejection control with the idea of cascaded fractional order integrator equivalence," *ISA Transactions*, vol. 114, pp. 359–369, 2021.

[27] D. Li, P. Ding, and Z. Gao, "Fractional active disturbance rejection control," *ISA Transactions*, vol. 62, pp. 109–119, 2016.

[28] S. Safiullah, A. Rahman, and S. Ahmad Lone, "Optimal control of electrical vehicle incorporated hybrid power system with second order fractional-active disturbance rejection controller," *Optimal Control Applications and Methods*, pp. 1–30, 2021.

[29] N. Li, "Research on high precision antenna pointing control algorithm," *Astronomical Research & Technology*, vol. 14, p. 4, 2017 (in Chinese).

[30] I. Podlubny, "Fractional differential equations [electronic resource]: an introduction to fractional derivatives, fractional differential equations, to methods of their solution and some of their applications," *Mathematics in Science and Engineering*, vol. 3, pp. 553–563, 2013.

[31] D. Xue, *Fractional Calculus and Fractional Control* SCIENCE PRESS, Beijing, China, 2018.

[32] A. Oustaloup, F. Levron, B. Mathieu, and F Nanot, "Frequency-band complex noninteger differentiator: characterization and synthesis," *IEEE Transactions on Circuits and Systems I: Fundamental Theory and Applications*, vol. 47, no. 1, pp. 25–39, 2000.

[33] I. Podlubny, *Fractional Differential Equations: An Introduction to Fractional Derivatives, Fractional Differential Equations, to Methods of Their Solution and Some of Their applications*, Elsevier, Amsterdam, Netherlands, 1998.

[34] X. L. Shao and H. L. Wang, "Performance analysis on linear extended state observer and its extension case with higher extended order," *Control and Decision*, vol. 30, no. (5), pp. 815–822, 2015.